Chapter 3

Infrared Nano-Focusing by a Novel Plasmonic Bundt Optenna

Ehab Awad

Abstract

Infrared optical detection devices such as photodetectors, solar cells, cameras, and microbolometers are becoming smaller in size with a tiny active area in the range of a few micrometers or even nanometers. That comes at the expense of a smaller aperture area of the device, and in turn inefficient collection of infrared energy. Therefore, infrared plasmonic optical antennas are becoming essential to efficiently collect optical energy from free space and concentrate it down to the device's tiny area. However, it is desirable to develop plasmonic antennas with a broad bandwidth, polarization insensitivity, wide field-of-view, and reasonable plasmonic losses. That ensures collection of most incident infrared radiation and enhancement of power absorption efficiency. In this chapter, some types of plasmonic antennas are explored with an emphasis on innovative type of optical antenna called Bundt Optenna. We investigate Bundt Optenna design and optimization. This antenna has a novel shape that looks like a Bundt baking pan and it is made of gold. Several Bundt unit cells can be arranged in a periodic array that is placed on top of a thin-film infrared absorbing layer. The Bundt Optenna utilizes surface plasmons to squeeze both electric and magnetic fields of infrared radiation down to a 50 nm wide area, thus enhancing absorption efficiency within an underneath thin-film layer. The Optenna demonstrates polarization insensitivity and ultra-broad bandwidth with a large fractional bandwidth within the near, short-wave, and mid-wave infrared bands. It also shows a remarkable enhanced power absorption efficiency and a wide field-of-view.

Keywords: nanophotonics, optical antenna, surface plasmonics, infrared detection, infrared absorption enhancement

1. Introduction

Infrared detectors have many types, which can be classified based on their applications and physical response to infrared radiation. Some of them are sensitive to temperature changes due to the thermal effects of infrared radiation, others absorb infrared photons and generate free carriers. Examples of infrared detectors are microbolometers, pyroelectric detectors, cameras, photodetectors, and solar cells [1].

Infrared detectors are becoming ultra-compact in size with tiny active areas in the range of a few micrometers or nanometers. That enhances as well as yields novel

detection characteristics and properties [2]. The tiny size has several advantages. It allows for efficient cooling of the detector, thus reducing thermal noise and allowing good performance at high temperatures. It reduces device capacitance and thus allows for ultrafast optical switching and manipulation of high bitrates data. Also, it permits the collection of almost all photogenerated carriers due to their short path to electrodes, and thus high quantum efficiency. In cameras and sensors, tiny size means aggregating a lot of small-size pixels in a small area, and thus high spatial resolution imaging and the possibility of ultra-dense integration.

Downsizing the detection devices area comes at the expense of the smaller aperture area, and in turn inefficient collection of infrared radiation energy. The solution to such a problem is to utilize infrared plasmonic optical antennas in front of the detectors. The optical antennas can collect optical energy efficiently from free space to focus it on small size devices [3–8]. The plasmonic focusing of electric fields into sub-wavelength nano hot spots increases the atoms absorption cross-section areas within detection material (e.g. thin-film) and in turn the materials absorption coefficient [8–19].

The optical antenna design should have some characteristics for getting the best performance. In other words, it should have a special shape, different stages, and optimum dimensions. The shape should be selected to have a large aperture that collects infrared energy from all over the free space and focuses it down to a sub-wavelength nanoscale area. One aspect of that is to minimize the back-reflections of optical energy at the antenna input. That can be done by matching the antenna input optical impedance to that of free-space, in addition to optical impedances among different stages of the antenna. That of course imposes a lot of constraints on antenna dimensions. Talking about optical impedance, we mean the wave nature of light that allows us to treat light as an electromagnetic wave with ultra-high frequency traveling in a medium with impedance.

The antenna should also have a special shape that allows it to be polarization-insensitive. In that way, it can collect infrared energy from different incident polarizations, which is useful, especially for solar cells and energy harvesting applications. However, it is worth mentioning that in some other applications like infrared cameras, for example, polarization-dependent (i.e. polarimetric) detection can be useful to distinguish between different features in a scene [20].

In addition, the plasmonic antenna should have an overall small size to minimize ohmic power losses associated with surface plasmon polaritons (SPP) traveling waves on antenna metal surfaces [21]. Moreover, the optical antenna should have a broad bandwidth. Thus, it can collect as much energy as possible within a specific wavelength band, and in turn, its average response over such particular bandwidth is maximized. Also, the optical antenna should have a wide field of view to collect as much radiation as possible from all angles of view.

It is worth mentioning that optical antennas are not solely useful in infrared detection applications. Optical nanoantennas can be also useful in detection applications within the visible range. For example, it can be used in energy harvesting and solar cells [22–24].

In the following sections, some examples of optical infrared antennas will be presented. In Section 2, a brief overview of some optical antenna examples will be discussed. In Section 3, a novel design of a plasmonic Bundt optical antenna will be presented and discussed. In Section 4, the performance of the Bundt optical antenna will be evaluated. Finally, a conclusion section will summarize the important points discussed in this chapter.

2. Examples of optical infrared antennas

There are various types of optical antennas that have been known so far. To name some, a half-wave dipole optical antenna can concentrate infrared onto nanometer germanium photodiode. This optical antenna is polarization sensitive. It covers a bandwidth of 1.34 to 1.48 μm and it shows a factor of 20 enhancement in detector response [8]. Another example is a silicon plasmonic horn that has periodic grooves on its surface. It has a short length and gives a maximum coupling efficiency of 27% within the wavelength range of 1538 to 1562 nm [9]. A silver nano-array of coaxial rings shows extraordinary transmission with almost a factor of 4 enhancement in transmitted optical intensity [10]. A hybrid silicon-gold nano-particles optical antenna is also demonstrated with multipole resonance. It covers all the visible wavelength range and can enhance optical absorption by a factor of 2.5 [11]. A plasmonic spiral ring grating could be coupled to a vertical nano-optical antenna to enhance optical field intensity by up to 7 orders of magnitude. The simulated collection efficiency can reach up to 68% [12]. A dielectric silicon nanoantenna is demonstrated with an ultra-low optical power loss and heating conversion. It covers the near-infrared band and can enhance surface fluorescence by about 3 orders of magnitude [13]. A trench thin metal polarization-insensitive antenna is demonstrated. It is polarization insensitive with high responsivity at tele-communication infrared wavelengths [14]. A nanoantenna sandwiched between two graphene monolayers photo-detector is demonstrated. It covers both visible and infrared bands with 8 times enhancement in detection response and up to 20% internal quantum efficiency [15].

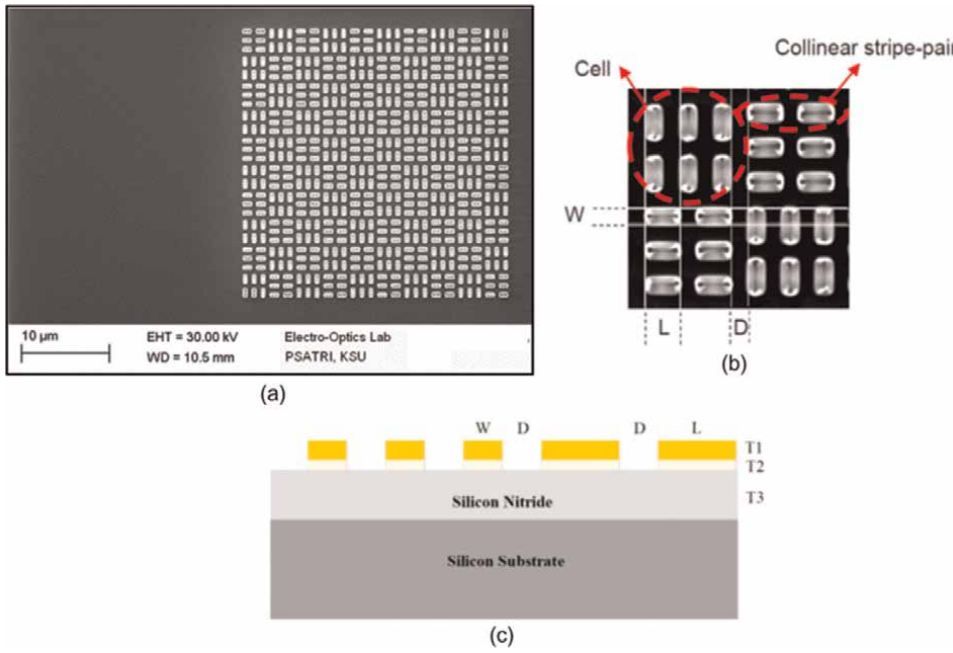

Figure 1.
The checkerboard optical antenna detection device. (a) the SEM image of the fabricated checkerboard device sample (30 x 30 μm²). (b) Magnified SEM image of four cross-oriented unit cells, L = 1049 nm, D = 530 nm, W = 510 nm. (c) a schematic cross-section in detection device, L = 1000 nm, W = 500 nm, D = 500 nm, T1 (gold) = 50 nm, T2 (titanium) = 10 nm, T3 (Si_3N_4) = 400 nm [16].

In the following subsections, structures of some types of optical antennas are explored and examined in detail.

2.1 Checkerboard optical antenna

The gold checkerboard antenna consists of nanoscale dipole antennas [16, 17]. **Figure 1a** and **b** show scanning electron microscope (SEM) images of such checkerboard structure. It consists of subwavelength gold stripes arranged in cross-oriented unit cells. The stripes are separated by subwavelength gaps. Each stripe acts like a dipole antenna that can receive long infrared radiation (8-12 μm). The gold stripes interact with incident light electromagnetic waves resulting in collective electrons oscillations (plasmons) in direction of light polarization (i.e. forming dipoles). The oscillating electrons accumulate at the stripes' edges resulting in a very high electric field with spatial nano-resolution [21]. These localized surface plasmons are coupled together within the gaps among stripes, thus creating what is called hot spots. These hot spots have very high concentrated infrared optical intensities. Thus, it can increase the optical absorption within the underneath absorbing layer of silicon

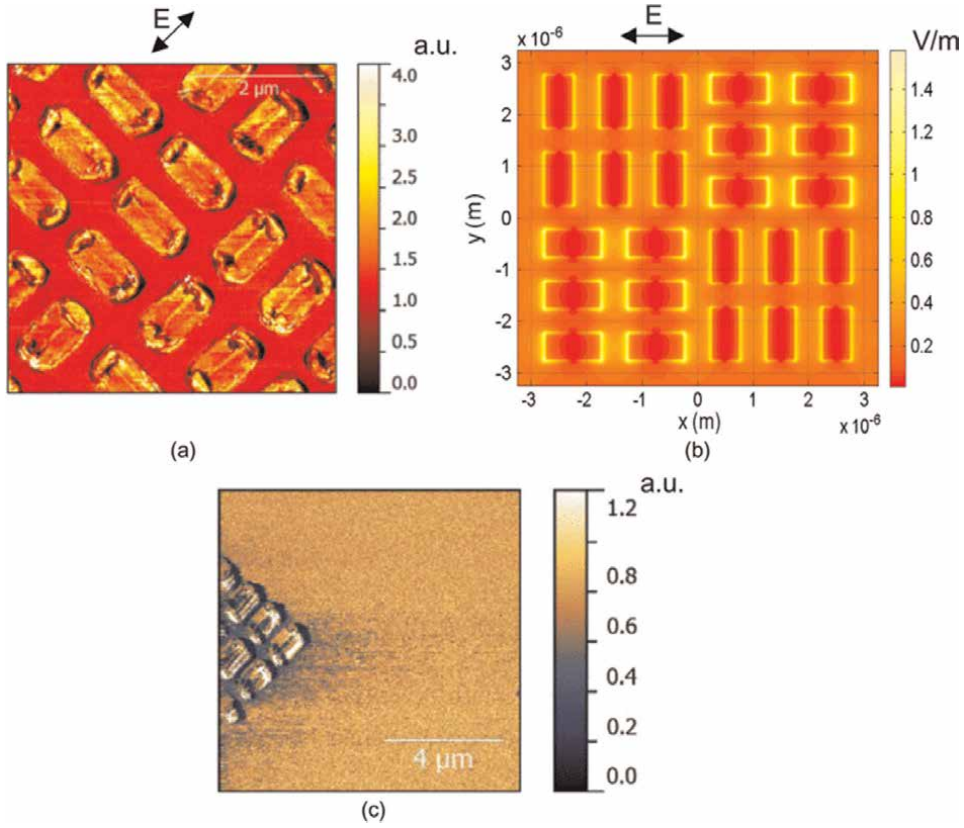

Figure 2.
(a) The SNOM image of the scattered electric field (E), in arbitrary units, from the checkerboard sample (rotated) at a 10.19 μm wavelength. (b) the FDTD simulation of scattered electric field magnitude under the same SNOM measurement conditions in part (a). (c) a comparison of the SNOM scattered electric field magnitudes with/ without checkerboard on the same sample at 10.6 μm wavelength [16].

nitride (Si_3N_4) and in turn the detection efficiency. The detection device layers structure is shown in **Figure 1c**.

Figure 2a and **c** show images of scattered electric fields from the checkerboard antenna taken by scanning near-field optical microscope (SNOM) at a wavelength of 10.19 μm. **Figure 2b** shows a corresponding image to that of **Figure 2a**, simulated using a three-dimensional finite-difference time-domain (FDTD) method. As seen in **Figure 2c**, there is a dark area underneath the checkerboard structure. This darkness indicates enhanced absorption within the silicon nitride thin-film layer.

The tested checkerboard antenna shows broadband and polarization-independent average absorption enhancement of 63.2% over the wavelength range 8–12 μm. Also, it shows a maximum absorption enhancement of 107% at 8 μm wavelength and a minimum enhancement of 24.8% at 12 μm wavelength.

2.2 Dipole nanoantenna coupled to plasmonic slot waveguide

Another example of optical antennas is the dipole coupled to a plasmonic slot waveguide [18]. The dipole antenna is made of gold and has a bottom and side reflectors that can increase its coupling efficiency up to 26% at a wavelength of 1550 nm. The coupling efficiency is defined as the ratio of power delivered to the waveguide to incident power on the dipole antenna. In this configuration the dipole antenna is irradiated by a vertical optical fiber terminated by a focusing lens, see **Figure 3a**.

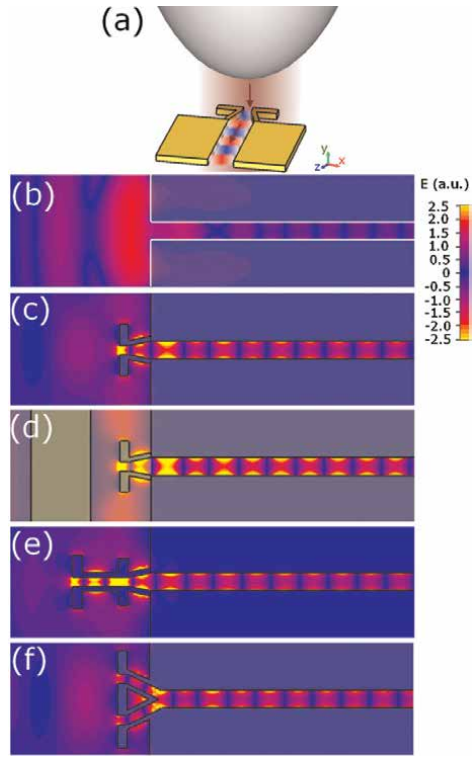

Figure 3.
(a) Antenna working in vertical coupling configuration. The beam from the fiber excites slot plasmons. Instant images of the simulated electric field (E) in arbitrary units at ?=1.55 μm when coupling to (b) waveguide only, (c) single antenna, (d) antenna with side and bottom reflectors, (e) serial, and (f) parallel antenna array. The color scale is equal for (b) through (f). Reprinted with permission from [ref 18] © the Optical Society.

The antenna collects fiber radiation and launches it inside an impedance-matched slot waveguide. The dipole antenna length is adjusted to be an integer number of half-wavelengths. Also, the side and bottom reflectors are positioned such that it forms a maximum of standing wave reflections at the antenna position. **Figure 3** shows different configurations of the tested system together with images of simulated electric fields. As seen, the coupled electric field magnitudes increase from **Figure 3a–d** here the coupling efficiency becomes maximum. The system is also tested with serial and parallel dipole arrays as shown in **Figure 3e** and **f**, respectively. However, these two configurations give the same performance as a single dipole antenna with side and bottom reflectors.

This dipole nanoantenna shows 185 times enhancement in coupling efficiency when compared to a bare waveguide. It can be utilized as an interface coupler between an optical fiber and a plasmonic slot waveguide.

2.3 Horn optical nanoantenna

An additional example of optical antennas is a two-dimensional plasmonic horn nanoantenna made of silver. This antenna is impedance matched to a plasmonic slot feeding transmission line [19]. It has a broad bandwidth (1260–1675 nm) for applications in wireless on-chip communications. It is investigated by FDTD simulations as shown in **Figure 4**. In **Figure 4a, d** and **g**, the horn length and its flare angle should be

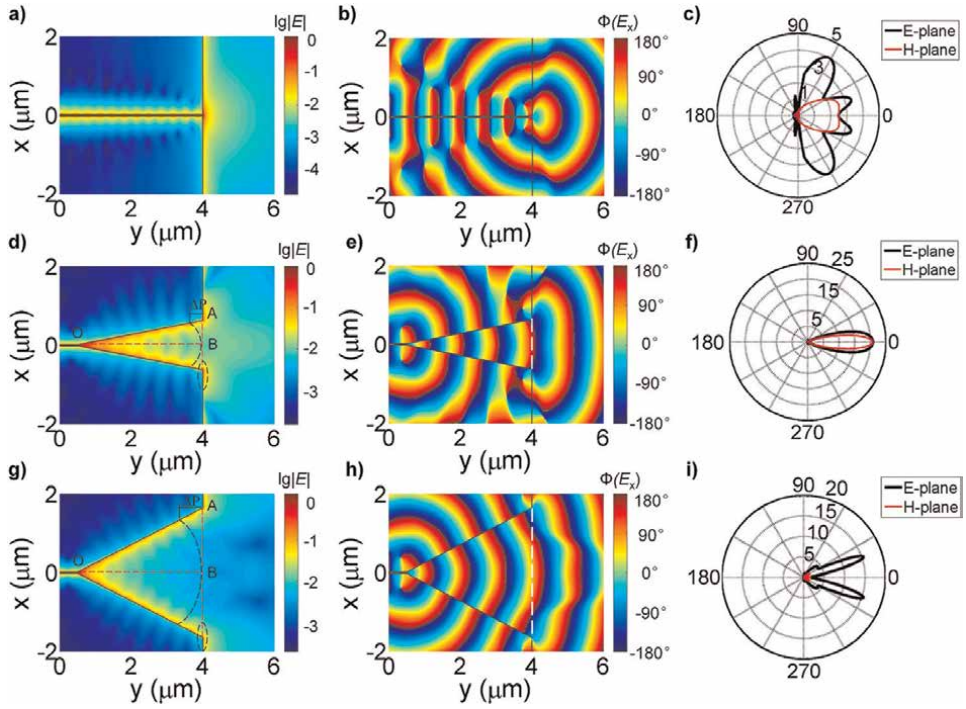

Figure 4.
Near-field profiles and far-field radiation patterns of a bare waveguide and horn nanoantennas with different flare angles. (a–c) Bare waveguide case. The amplitude (a), phase (b) of electric field distribution, and radiation pattern (c) of a bare waveguide. (d–f) a horn nanoantenna with a length (L_a) of 3.5 μm and flare angle (θ) of 10°. The amplitude (d), phase (e) of electric field distribution, and radiation pattern (f). (g–i) a horn nanoantenna with L_a = 3.5 μm and θ = 25°. The amplitude (g), phase (h) of electric field distribution, and radiation pattern (i) [19].

carefully designed to minimize back reflections at the horn input. The corresponding wavefront phase distributions are shown in **Figure 4b, e,** and **h**. In **Figure 4c, f,** and **i**, the far-field radiation patterns are shown for each case. The best design is found to be the case in **Figure 4d–f**, where the back-reflected field magnitude is minimized, the phase front looks like a plane-wave, and thus it is matched to that of free-space radiation, in addition, the radiation pattern is highly directional. This optical antenna can give a superior performance with almost 100-fold enhancement in power transfer when compared to conventional dipole nanoantennas.

It is worth mentioning that an optical antenna design should take into consideration some points that allow it to have better performance characteristics when compared to the previous designs. For example, it should have a special shape with a large aperture to collect infrared energy from all free-space and focuses it on a nanoscale area. Also, back-reflections of antenna optical energy should be minimized by matching antenna input optical impedance to that of free-space. That of course imposes a lot of design constraints on the optical antenna dimensions. It is also better to have a polarization-insensitive antenna to collect all infrared energy at different polarizations. In addition, a plasmonic optical antenna should be small enough to minimize the surface plasmon polaritons' ohmic power losses. It is also desirable to have a broadband antenna optical response. Moreover, an optical antenna should have a wide field of view to collect optical energy from all over free-space angles.

In the following sections, we will explore in detail a novel optical antenna called Bundt Optenna that realizes these design constraints and thus possess several advantages.

3. Bundt plasmonic antenna

Now we are going to examine a novel optical antenna design that is called Bundt Optenna [25, 26]. Here, the optical antenna is abbreviated as "Optenna" and has a unique shape that looks like a Bundt baking pan. The Bundt Optenna has been featured by scientific media as promising for nanoscale infrared detection devices such as solar cells, telecommunications photodetectors, shortwave cameras, and mid-wave microbolometers [27]. In addition, it can keep plasmonic losses to a minimum while focusing infrared radiation to nanoscale size, thus doing the trick [28].

This Bundt Optenna has many desirable advantages. It has an ultra-broadband optical response covering the near, shortwave, and mid-wave infrared bands with high fractional bandwidth up to 42%. It is polarization insensitive with a wide field of view. It can squeeze both electric and magnetic fields down to 50 nm spot area to enhance optical absorption efficiency within a thin-film detection layer. The power absorption enhancement can reach up to 8 orders of magnitude (i.e. 80 dB). Moreover, it has a compact size with potential applications in energy harvesting, optical communications, and biomedical technology.

Figure 5 shows a schematic diagram of the Bundt Optenna structure with different cross-sections. It has a gold concentric structure that is filled with air as a dielectric material. The Optenna is built on top of a semiconductor thin-film detection layer above a thick bulk substrate. **Figure 5a** shows a two-dimensional periodic array of the Bundt unit-cells with a periodic separation of "L". A vertical cross-section in a single unit cell is shown in **Figure 5b**. It shows three stages. The first stage consists of a

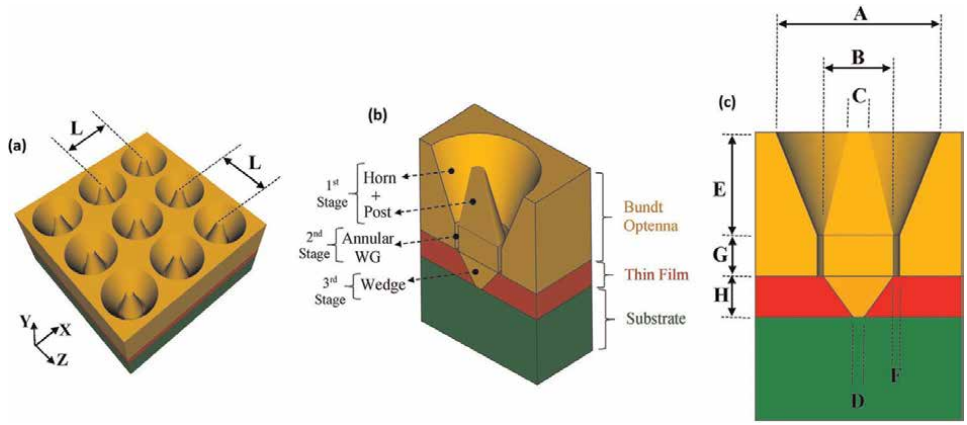

Figure 5.
The schematic diagram of the proposed infrared detection device with Bundt Optenna. (a) a perspective view of 2D periodic Bundt array, (b) a vertical cross-section of unit-cell indicating different stages and the underneath semiconductor layers, (c) a vertical cross-section of unit-cell indicating different dimensions [25].

coaxial (concentric) conical horn and a middle post. The conical concentric shape allows the Optenna to easily impedance match surrounding free-space, and collect most of the incident radiation due to its relatively large input aperture. In addition, this shape allows for polarization-insensitive operation because of its symmetry around the central axis. The second stage is an annular gold waveguide that matches the optical impedance between the first stage and the third stage. The third stage is a conical gold wedge extending through the thin-film detection layer. It allows the excited SPP to penetrate deep inside the absorbing layer thus increasing the overall absorption area inside the thin-film. **Figure 5c** labels different dimensions on the cross-section of a single unit cell.

The incident free-space infrared radiation is collected by the Bundt array's large aperture. The coaxial horn and post with air-filling dielectric act like a metal–insulator–metal (MIM) waveguide that has a conical flare. This waveguide is end-fire excited by incident free-space radiation and generates SPP on the antenna gold surfaces forming a TE_{11} mode [29] that propagates along the MIM waveguide. Both the plasmonic electric and magnetic fields are squeezed gradually during propagation until they reach a sub-wavelength nano wide (F = 50 nm) annular area at the first stage output. This area can be found by the following equation:

$$\text{Area} = \pi \times \left[\left(\frac{B}{2} + F\right)^2\right] - \left(\frac{B}{2}\right)^{2.} \tag{1}$$

The "A", "B", "C", and "E" are the dimensions of Bundt's first stage. They are optimized to allow optical-impedance matching between free-space and Bundt coaxial horn. This means the optical bac-reflections are minimized, and in turn forward propagating transmitted signals are maximized. An annular waveguide with a width "F" and length "G" that is filled with air is used as an intermediate second stage. Which matches the optical impedance between the antenna's first stage and third stage (absorbing thin-film). The annular waveguide is an extension of the flared coaxial horn with TE_{11} propagating squeezed mode. The annular waveguide has multiple reflections between its input and output like a Fabry-Perot resonator. Therefore,

the waveguide length "G" is chosen to make the round-trip phase-shift (Δφ) equal to "mπ". This condition can be written as:

$$\Delta\varphi = 2 \times G \times K + \delta\varphi = m \times \pi \tag{2}$$

The "δφ" is the reflections phase-shift at waveguide input and output, "k" is the propagation constant, and "m" is an integer number. This condition results in constructive interference at waveguide output, and destructive interference of back-reflected waves at waveguide input.

The third stage of the Bundt Optenna is a conical gold wedge of length "H", besides the Bundt base on top of the thin-film layer. The third stage acts like a flared MIM waveguide that is excited by the SPP out of the annular waveguide. This SPP spreads inside the absorbing thin-film layer. Therefore, the third stage allows excited SPP to penetrate and spread deep inside the thin-film, thus increasing the overall absorption area of the absorbing layer.

The Bundt Optenna array was designed and simulated over different infrared bands. That includes near-infrared (NIR), short-wave infrared (SWIR), and mid-wave infrared (MWIR) wavelengths bands. The dimensions of different Bundt stages are optimized during numerical simulations to get the best optical impedance matching. That means minimizing back reflections and maximizing transmission to obtain an almost flat response. We obtain four designs of the Bundt Optenna. Each design has specific dimensions. **Table 1** summarizes the dimensions of each design. It is found that there are some rules which should be satisfied in all these designs. The coaxial horn length "E" should be greater than the maximum wavelength of each design range. That is to ensure having one electric-field cycle along the horn length. Also, the inner perimeter of the annular waveguide (i.e. π × B) should be greater or equal to the maximum wavelength of the corresponding range. That ensures the magnetic field one period around the waveguide perimeter is not smaller than the maximum wavelength of TE_{11} mode. To minimize ohmic loss of SPP, the "E" dimension and (π × B) are selected to be equal to the maximum wavelength. The dimension "A" is chosen to maintain a symmetric coaxial horn. The dimensions "C", "D", "G", and "L" are chosen by numerical iterations to minimize back-reflections. The largest Bundt unit-cell 3.25x3.25x6.8 μm^3 is for the MWIR design. While the largest unit-cell aspect ratio 3.6:1 is for the NIR design. The Bundt has an overall compact size with a reasonable aspect ratio. The Optenna designs "1", "2", "3", and "4" are useful in applications such as solar cells, optical communications photodetectors, SWIR sensors/ cameras, and MWIR thermal detection/ imaging with microbolometers, respectively.

Band	Range (μm)	Design	A	B	C	D	E	G	L
NIR	0.74–1	**1**	0.6	0.32	0.05	0.125	1	0.5	0.625
SWIR	1 – 2	**2**	1.4	0.7	0.05	0.25	2	1	1.425
	2 – 3	**3**	2	1	0.1	0.35	3	0.5	2.025
MWIR	3 – 5	**4**	3.2	1.6	0.2	0.55	5	1	3.25

*The assigned dimensions' are already indicated in **Figure 1**, and they are measured in "μm". The dimensions H = 0.7 μm and F = 50 nm are fixed for all the designs [25].*

Table 1.
The four designs of Bundt Optenna that can cover the three infrared bands.

4. Bundt plasmonic Optenna performance

The Bundt Optenna performance is evaluated using three-dimensional FDTD. The thin-film layer is selected to be silicon nitride as an example, with a silicon substrate. **Figure 6** shows the normalized magnitudes of the electric (magnetic) fields of one unit cell. The wavelength is selected here to be 2.3 μm with TM linear polarization along the x-direction. **Figure 6a** shows a vertical cross-section of a unit-cell (X-Y plane) at Z = 0. As shown, the SPP electric-fields inside the concentric horn are concentrated around the post as it has a small apex angle. The highest electric-field intensity is found to be within the 50 nm wide annular waveguide. Inside the thin-film layer, the high-intensity field propagates and spreads with more SPP concentration around the wedge and Bundt base. This high-intensity field is absorbed and exponentially attenuated within the thin-film layer. It almost vanishes within the underneath silicon substrate. The back-reflected electric-field is very small. A supplementary Video 1 (https://bit.ly/3t8Bundt) illustrates the electric-field propagating at 2.3 μm wavelength inside the Bundt Optenna.

Figure 6b–d illustrate the electric-field at cross-sections X-Z at Bundt annular waveguide input and output, respectively. They show the TE_{11} squeezing down to 50 nm wide annular area at the thin-film layer. **Figure 6–b** shows the TE_{11} mode normalized electric-filed at concentric horn input. **Figure 6c** shows the squeezed TE_{11} plasmonic electric-field at the annular waveguide input. The maximum normalized electric-field is 8 at the annular waveguide. Which is almost eight times enhancement in the field strength (i.e. 18 dB). **Figure 6e** illustrates the squeezed magnetic TE_{11}

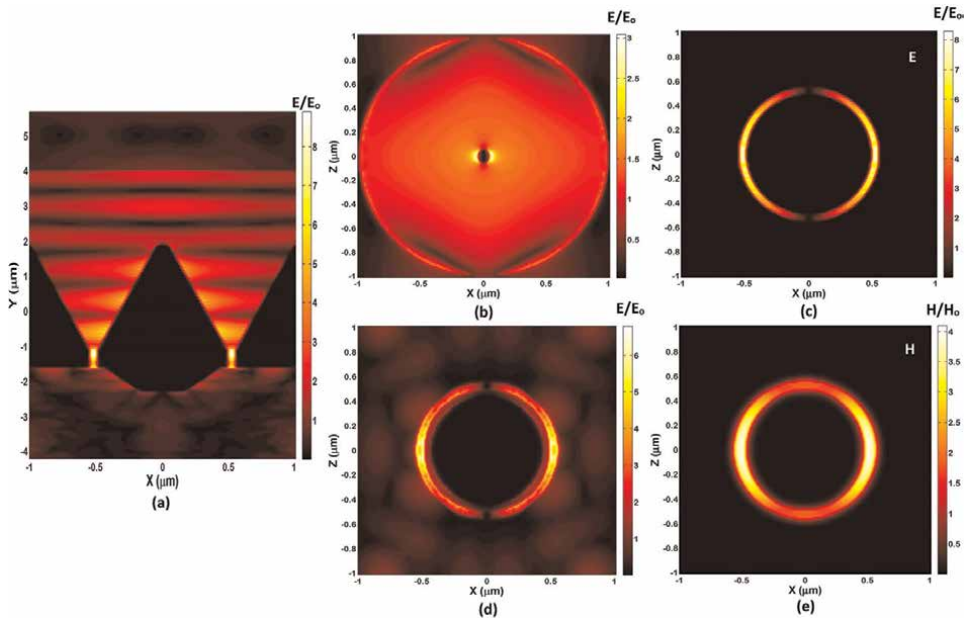

Figure 6.
The three-dimensional FDTD simulations fields (normalized) within a unit-cell of infrared detection device at a wavelength of 2.3 μm, and TM incident polarization. The normalized electric-field magnitude (E/E_o): (a) a vertical cross-section in a unit-cell, (b) a horizontal cross-section at the input of concentric horn, (c) a horizontal cross-section at the input of annular waveguide, (d) a horizontal cross-section just outside the annular waveguide (i.e. at the entrance of the thin-film layer. The normalized magnetic-field magnitude (H/H_o): (e) a horizontal cross-section at the input of the annular waveguide [25].

plasmonic -field magnitude at the annular waveguide input. It has a maximum of 4, which indicates ≅12 dB improvement in the field strength. **Figure 6d** shows the nano-focused electric-field at the entrance of the thin-film layer, where the electric-field strength starts to attenuate by optical absorption.

Figure 7 illustrates the coupling ratio (CR) of TM-polarization in each Bundt Optenna stage versus wavelength. Figures (a), (b), (c), and (d) correspond to designs "1", "2", "3", and "4", respectively. The CR is defined as the ratio of transmitted power at each stage to input power. The CR into stage "1" is considerably high for all designs. However, it does not reach zero dB due to small back-reflections into free-space. The back-reflections are estimated to be less than −7 dB. The CR within the third stage shows a high collection efficiency of the Optenna. The CR of the second and third stages is less than the first stage due to SPP ohmic power loss on gold surfaces. The 3 dB bandwidth (BW) of Bundt Optenna is measured at Optenna third stage because it is the transferred power by the optenna to thin-film layer. The small ripples on curves are due to the Fabry-Perot effect at different interfaces of Optenna stages. **Table 2** shows the bandwidth for each Bundt design together with its center-wavelength (λ_o) and calculated optical fractional bandwidth (O-FBW). The O-FBW is the ratio of bandwidth to center-wavelength (i.e. BW/λ_o). The table shows a broad-band optical response with a high optical fractional bandwidth ≅ 35% up to 42%.

It is worth noting the following issues regarding the Bundt Optenna performance. The field squeezing results in a dramatic reduction in its cross-section area, which

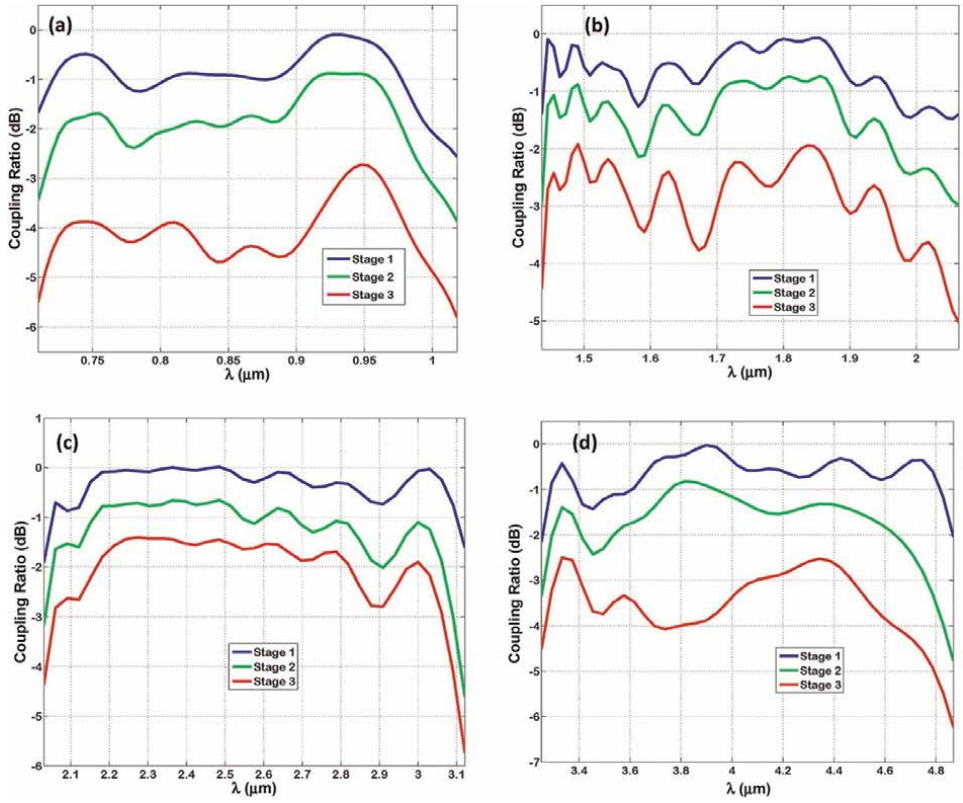

Figure 7.
The coupling ratio estimated in decibels of TM-polarized infrared radiation at successive stages of Bundt Optenna: (a) design "1", (b) design "2", (c) design "3", (d) design "4" [25].

Band	Design	Wavelength (μm)	BW (μm)	λ_o (μm)	O-FBW (%)
NIR	1	0.71–1.01	0.3	0.86	34.9
SWIR	2	1.43–2.06	0.63	1.75	36
	3	2.03–3.12	1.1	2.58	42.6
MWIR	4	3.25–4.86	1.61	4.06	39.7

In addition to the percentages of optical fractional bandwidth (O-FBW) [25].

Table 2.
The wavelength range, bandwidth (BW), and center-wavelength (λ_o) of different Bundt designs, measured in micrometer (μm).

means a high gain in optical intensity despite power attenuation by SPP ohmic losses. The intensity is defined as the optical power divided by area. The nano-focused fields' intensity increases the effective absorption cross-section area of material atoms, and thus the materials absorption coefficient. Therefore, the thin-film absorption efficiency is expected to increase because of Bundt's high intensity that reaches, for example, 12.4 dB at the wavelength of 3.3 μm. The average ohmic losses on gold surfaces due to SPP are found to be almost -3 dB, which is considered reasonable. The different Bundt designs are found to be polarization insensitive over different tested bands. That is due to the two-dimensional symmetry of the Bundt structure. Therefore, the Bundt optical response is always the same for all types of incident polarizations. That is advantageous as Optenna can collect most of the incident radiation power regardless of its polarization. Moreover, the Bundt field of view is measured by varying radiation incidence angles while monitoring the output intensity. For all the designs, the maximum incidence angle is found to be ≅40°, indicating a Bundt Optenna field-of-view ≅ 2 × 40° ≅ 80°.

Figure 8 illustrates the absorption enhancement factor (EF) inside the thin-film layer. It is defined as the ratio between thin-film absorbed power in the case with and without Bundt Optenna. It is measured in linear scale and decibels as well. The absorption EF is high and reaches a maximum of ≅8.5, 29, 80, and 15 dB for designs "1", "2", "3", and "4", respectively. The smallest EF is ≅2 dB at the band edges. The high EF of designs "2" and "3" are because of the very small attenuation coefficients of a silicon nitride material. Thus, the power absorption EF becomes significant due to Optenna. It can reach as high as ≅80 dB at a wavelength of ≅2.2 μm. The ripples on some curves are because of the Fabry-Perot effect due to residual multiple reflections among Optenna different stages. The enhanced absorption efficiency of the thin film layer is mainly due to the improved material absorption coefficient as the incident optical field intensities become much higher.

5. Conclusions

In this chapter, we have explored some types of plasmonic optical antennas that can focus optical infrared radiation to very small spot areas beyond the light diffraction limit. These antennas are essential for infrared optical detection devices that have tiny active areas in the range of a few micrometers or even nanometers. In addition, we have focused on one innovative type of optical antenna called Bundt Optenna. We investigated its design and optimization. The Bundt Optenna bandwidth covers the near-infrared, short-wave, and mid-wave infrared bands. The Bundt has a wide

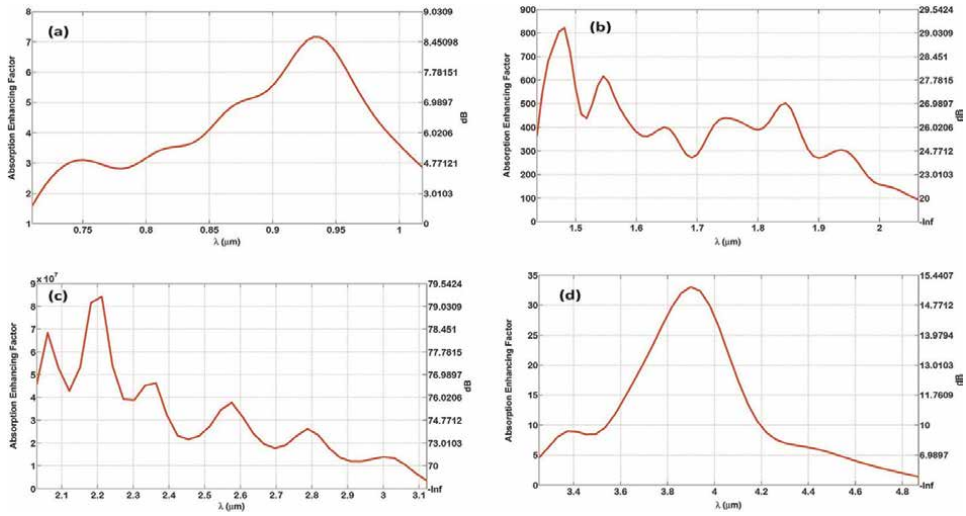

Figure 8.
The Bundt Optenna absorption enhancement factor inside the thin-film layer indicated in linear scale on the left axis, and in decibels on the right axis: (a) design "1", (b) design "2", (c) design "3", (d) design "4" [25].

field-of-view equal to 80°. It has an ultra-broadband optical response and fractional bandwidth of up to 42%. It can nano-focus electric and magnetic fields to a 50 nm-wide area, and thus enhance the optical absorption efficiency of the thin-film detection layer. The fields' intensity gain can reach up to 12.4 dB. The power absorption enhancement can be 8 orders of magnitude (i.e. 80 dB). The average ohmic power loss in Bundt Optenna is as low as −3 dB. The Optenna is polarization-insensitive and has a relatively compact size. The Bundt Optenna can be used in different nanoscale detection devices such as photodetectors, solar cells, cameras, and microbolometers, with potential applications in optical communications, imaging, energy harvesting, optical sensors, and biomedical technology.

Video materials

Video 1 available from https://bit.ly/3t8Bundt

Author details

Ehab Awad
Electrical Engineering Department, College of Engineering, King Saud University, Riyadh, Saudi Arabia

*Address all correspondence to: esawad@ieee.org

IntechOpen

© 2022 The Author(s). Licensee IntechOpen. This chapter is distributed under the terms of the Creative Commons Attribution License (http://creativecommons.org/licenses/by/3.0), which permits unrestricted use, distribution, and reproduction in any medium, provided the original work is properly cited. CC BY